Published in final edited form as:

Acta Crystallogr F Struct Biol Commun. 2020 September 01; 76(Pt 9): 428–437. doi:10.1107/S2053230X20010250.

Binding of Inhibitors to Active Site Mutants of CD1, the Enigmatic Catalytic Domain of Histone Deacetylase 6

Jeremy D. Osko, **David W. Christianson***

Roy and Diana Vagelos Laboratories, Department of Chemistry, University of Pennsylvania, 231 South 34th Street, Philadelphia, PA 19104-6323, United States.

Abstract

The zinc hydrolase histone deacetylase 6 (HDAC6) is unique among vertebrate deacetylases in that it contains two catalytic domains, designated CD1 and CD2. Both domains are fully functional as lysine deacetylases *in vitro*. However, the *in vivo* function of only the CD2 domain is well defined, whereas that of CD1 is more enigmatic. We now report three X-ray crystal structures of HDAC6 CD1–inhibitor complexes to broaden our understanding of affinity determinants in the active site. Notably, cocrystallization with inhibitors was facilitated by using active site mutants of zebrafish HDAC6 CD1. The first mutant studied, H82F/F202Y HDAC6 CD1, was designed to mimic the active site of human HDAC6 CD1. The structure of its complex with Trichostatin A was generally identical to that with the wild-type zebrafish enzyme. The second mutant studied, K330L HDAC6 CD1, was prepared to mimic the active site of CD2. We previously demonstrated that this substitution does not perturb inhibitor binding conformations to HDAC6 CD1; here, this mutant facilitated cocrystallization with derivatives of the cancer chemotherapy drug suberoylanilide hydroxamic acid (SAHA). These crystal structures allow us to map out inhibitor binding regions in the outer active site cleft, where one HDAC isozyme typically differs from another. We expect that these structures will help guide the structure-based design of inhibitors with selectivity against HDAC6 CD1, which in turn will enable new chemical biology approaches to probe its cellular function.

Graphical Abstract

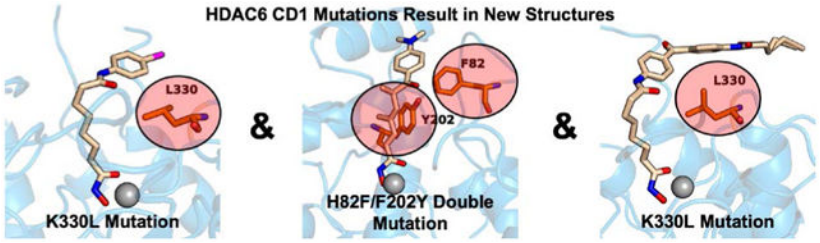

*Correspondence: chris@sas.upenn.edu.

Credit authorship contribution statement

All authors contributed equally to this work.

Declaration of competing interest

The authors declare no competing financial interests.

Keywords

zinc enzyme; hydrolase; enzyme inhibitor; drug design

1. Introduction

The biological functions of many proteins are regulated by enzyme-catalyzed lysine acetylation-deacetylation cycles (Choudhary et al., 2009; Verdin et al., 2015), and histone deacetylases play a prominent role in this regulatory strategy (López et al., 2016; Porter and Christianson, 2019). These enzymes are named for their ability to catalyze the deacetylation of nuclear histone proteins, the acetylation of which was first discovered nearly 60 years ago (Allfrey et al., 1964). However, this enzyme nomenclature is somewhat misleading, in that histone deacetylase substrates include not only histone proteins but also thousands of other proteins in various subcellular locations (Hornbeck et al., 2015). For example, histone deacetylase 6 (HDAC6) operates predominantly in the cell cytosol (Verdel and Khochbin, 1999; Grozinger et al., 1999), where its substrates include α-tubulin (Hubbert et al., 2002; Zhang et al., 2003; Li and Yang, 2015) and Tau (Min et al., 2010; Cohen et al., 2011; Noack et al., 2014; Carlomagno et al., 2017; Tseng et al., 2017). The HDAC6-mediated deacetylation of α-tubulin is required for proper microtubule dynamics, and deacetylation of Tau influences phosphorylation and aggregation.

Human HDAC6 (Uniprot Q9UBN7) is a 1215-residue zinc-dependent hydrolase containing two catalytic domains, CD1 and CD2 (Verdel and Khochbin, 1999; Grozinger et al., 1999; Zhang et al., 2006; Zou et al., 2006). Amino acid side chains required for the chemistry of catalysis are strictly conserved between CD1 and CD2: a tyrosine side chain assists the zinc ion in polarizing the scissile carbonyl group of the substrate, and tandem histidine residues serve general base-general acid functions (Lombardi et al., 2011; López et al., 2016; Porter and Christianson, 2019). However, the substrate specificity of CD1 is much narrower than that of CD2 due to amino acid substitutions in the active site; moreover, the narrow substrate specificity of HDAC6 CD1 from *Homo sapiens* (human) is even more stringent than that of HDAC6 CD1 from *Danio rerio* (zebrafish) as measured using single- or di-domain enzyme constructs (Hai and Christianson, 2016; Osko and Christianson, 2019). Curiously, a recent study of full-length human HDAC6 suggests wider substrate specificity for CD1 (Kutil et al., 2019), so further studies of both CD1 and CD2 are required to fully understand structure-function relationships.

To enable structure-based inhibitor design strategies, the X-ray crystal structures of human HDAC6 CD2 and zebrafish HDAC6 CD1 and CD2 have been reported along with structures of selected enzyme-inhibitor complexes (Hai and Christianson, 2016; Miyake et al., 2016). Human HDAC6 CD1 was refractory to crystallization; moreover, even though human HDAC6 CD2 yielded a crystal structure, crystals were inferior to those of the zebrafish enzyme. Thus, X-ray crystallographic studies of HDAC6 CD1 and CD2 have relied on the zebrafish enzyme as a surrogate for the human enzyme. More than fifty structures of zebrafish HDAC6 CD2-inhibitor complexes have since appeared in the literature (Osko et al., 2020; Bhatia et al., 2018; Mackwitz et al., 2018; Porter et al., 2017; Porter et al., 2018;

Porter, Osko, et al., 2018; Porter, Shen et al., 2018; Shen et al., 2020). In contrast, only seven additional crystal structures of zebrafish HDAC6 CD1-inhibitor complexes have since been reported (Osko and Christianson, 2019). These structures illuminate active site features that contribute to inhibitor affinity and selectivity. In light of the structural differences between human and zebrafish HDAC6 CD1, as well as structural differences between HDAC6 CD1 and CD2, a deeper understanding of active site binding determinants is needed to inform inhibitor design strategies.

In order to broaden our understanding of inhibitor binding to HDAC6 CD1, we now report three new X-ray crystal structures of zebrafish HDAC6 CD1 mutants complexed with inhibitors containing hydroxamate zinc-binding groups (Fig. 1). First, we report the crystal structure of H82F/F202Y HDAC6 CD1 complexed with the natural product inhibitor Trichostatin A. The H82F and F202Y substitutions convert the active site of the zebrafish enzyme into a mimic of the human enzyme active site. Since the binding conformation of Trichostatin A does not change significantly in complex with the mutant, the structure of this complex verifies that the zebrafish enzyme serves as a valid surrogate of the human enzyme. Finally, we report two crystal structures of K330L HDAC6 CD1 complexed with derivatives of suberoylanilide hydroxamic acid (SAHA), a drug currently in clinical use for cancer chemotherapy (Richon et al., 1996; Marks, 2007). These structures provide the first view of SAHA-based inhibitor binding in the HDAC6 CD1 active site, illuminating features of the protein landscape beyond the immediate active site that contribute to inhibitor binding.

2. Materials and methods

2.1. Reagents

All chemicals and buffers were purchased from Fisher, Millipore Sigma, or Hampton Research and used without further purification. The inhibitors Trichostatin A, SAHA-BPyne, and 4-iodo-SAHA were purchased from Caymen Chemicals and used without further purification (each compound was listed with >98% purity).

2.2. Preparation of *Danio rerio* HDAC6 CD1 mutant plasmids

The HDAC6 gene from *D. rerio* (residues 60-798, Uniprot F8W4B7) was synthesized by Genscript and the CD1 catalytic domain (residues 60-419) was recombinantly expressed in *Escherichia coli* using a pET-28a(+) vector. The gene sequence was optimized for *E. coli* expression. The genes for the H82F/F202Y HDAC6 CD1 and K330L HDAC6 CD1 mutants were similarly prepared by Genscript using PCR mutagenesis. Both of these constructs utilized a NdeI/BAMHI cloning site and contained kanamycin bacterial resistance. By nature of the pET-28a(+) vector, His tags were located at both the N-terminus and C-terminus with an N-terminal thrombin cleavage site. The final constructs utilized for crystallization are summarized in Table 1.

2.3. Expression and purification of *Danio rerio* HDAC6 CD1 mutants

The expression and purification of *Danio rerio* (zebrafish) HDAC6 CD1 was completed as recently described for wild-type and mutant enzymes (Osko and Christianson, 2019). To briefly summarize, *E. coli* One Shot BL21(DE3) cells (Invitrogen) were used for protein

expression and grown in 2xYT medium with 50 μg/mL kanamycin. Cells were grown in an Innova 40 incubator shaker at 37 °C and 250 rpm until OD_{600} reached approximately 0.80. The temperature was then decreased to 18 °C until OD_{600} reached 1.0. At OD_{600} of 1.0, the cells were supplemented with 400 μM isopropyl β-L-1-thiogalactopyranoside (IPTG; Gold Biotechnology) and grown for an additional 18 h at 250 rpm. Lastly, cells were centrifuged using a Sorvall LYNX 6000 centrifuge at 5000 rpm for 20 min. Cell pellets were stored at −80 °C until further use.

Prior to purification, the cell pellet was thawed and resuspended in 100 mL of buffer A [50 mM K_2HPO_4 (pH 8.0), 1 mM tris(2-carboxyethyl)phosphine (TCEP), 300 mM NaCl, 30 mM imidazole, and 5% glycerol]. Two protease inhibitor tablets, 0.1 mg/mL lysozyme, and 50 μg/mL DNase were added to the solution. Sonification was used to lyse the cells and the cell lysate was centrifuged using a Sorval LYNX 6000 centrifuge for 1 h at 15000 rpm. Once complete, the lysate was applied to a 5 mL pre-equilibrated HisTrap HP column.

Buffer B [50 mM K_2HPO_4 (pH 8.0), 1 mM TCEP, 300 mM NaCl, 300 mM imidazole, and 5% glycerol] was used to elute the His-tagged HDAC6 CD1 protein bound to the HisTrap HP column. All CD1-containing fractions were concentrated using a 15 mL centrifugal filter unit with a molecular weight cutoff of 10 kDa to 5 mL. The protein was then filtered using a 0.22 μM Millex-GV filter unit prior to being loaded onto a HiLoad Superdex 26/600 200 pg column. The column was pre-equilibrated with 360 mL of buffer C [50 mM 4-(2-hydroxyethyl)piperazine-1-ethanesulfonic acid (HEPES) (pH 7.5), 100 mM KCl, 1 mM TCEP, and 5% glycerol]. The 5 mL sample of HDAC6 CD1 protein was injected at a rate of 1 mL/min, and 5 mL fractions were collected. Pure “humanized” H82F/F202Y and K330L HDAC6 CD1 proteins were confirmed by sodium dodecyl sulfate−polyacrylamide gel electrophoresis, concentrated to approximately 10 mg/mL, and stored at −80 °C.

2.4. Crystallization of HDAC6 CD1 mutant–inhibitor complexes

The crystallization of zebrafish HDAC6 CD1 mutants complexed with inhibitors was achieved by sitting drop vapor diffusion, as recently described for cocrystallization with a different series of inhibitors (Osko and Christianson, 2019). Briefly, a 100-nL drop of protein solution [10 mg/mL HDAC6 CD1 mutant, 50 mM HEPES (pH 7.5), 100 mM KCl, 5% glycerol (v/v), 1 mM TCEP, and 2 mM inhibitor] was added to a 100-nL drop of precipitant solution and equilibrated against 80 μL of precipitant solution in the well reservoir of a 96-well PS MRC crystallization plate using a Mosquito crystallization robot (TTP Labtech).

For cocrystallization of the H82F/F202Y HDAC6 CD1–Trichostatin A complex, the precipitant solution was 0.2 M potassium acetate and 20% PEG 3350. For cocrystallization of the K330L HDAC6 CD1–SAHA-BPyne complex, the precipitant solution was 0.2 M potassium sodium tartrate tetrahydrate and 20% PEG 3350. For cocrystallization of the K330L HDAC6 CD1–4-iodo-SAHA complex, the precipitant solution was 0.2 M magnesium chloride hexahydrate and 20% PEG 3350. Crystals of each enzyme-inhibitor complex formed within 2–3 days at 21° C (room temperature) and were soaked in their respective mother liquors augmented with 20% ethylene glycol prior to flash-cooling. Crystallization parameters are summarized in Table 2.

2.5. Data collection, data reduction, and crystal structure determinations

X-ray diffraction data were collected on Northeastern Collaborative Access Team (NE-CAT) beamline 24-ID-C at the Advanced Photon Source (APS) from crystals of the H82F/F202Y HDAC6 CD1–Trichostatin A complex. A PILATUS 6M-F detector with an incident X-ray beam wavelength of 0.98 Å and temperature of 100 K was used for data collection. A full 180° of data were collected at a detector distance of 300 mm, in 0.20° angle increments, and 0.20 s exposure periods.

X-ray diffraction data were collected on beamline 17-ID-1 (AMX) at the National Synchrotron Light Source II (NSLS-II) from crystals of the K330L HDAC6 CD1–SAHA-BPyne complex. A Dectris Eiger 9M detector with an incident X-ray beam wavelength of 0.92 Å and temperature of 100 K was used for data collection. A full 180° of data was collected at a detector distance of 230 mm, in 0.20° angle increments, and 0.02 s exposure periods.

X-ray diffraction data were collected on NE-CAT beamline 24-ID-E at APS from crystals of the K330L HDAC6 CD1–4-iodo-SAHA complex. A Dectris Eiger 16M detector with an incident X-ray beam wavelength of 0.98 Å and temperature of 100 K was used for data collection. A full 180° of data was collected at a detector distance of 150 mm, in 0.20° angle increments, and 0.20 s exposure periods. Although the completeness and redundancy of this dataset were lower than expected, the structure of this complex ultimately refined satisfactorily and yielded excellent electron density maps. All data collection statistics are recorded in Table 3.

The CCP4 program suite (Winn et al., 2011) was used for data reduction for all three structures. All data were indexed using the CCP4 program iMosflm (Battye et al., 2011) and scaled using Aimless (Evans and Murshudov, 2013). The initial electron density map of each enzyme-inhibitor complex was phased by molecular replacement using the atomic coordinates of HDAC6 CD1 (PDB 5EEF) (Hai and Christianson, 2016) as a search probe with Phaser (McCoy et al., 2007). The interactive graphics program Coot (Emsley et al., 2010) was used to build and manipulate atomic models of each enzyme-inhibitor complex. Crystallographic refinement was performed using Phenix (Adams et al., 2010). Final refined structures were validated using MolProbity (Chen et al., 2010) prior to deposition in the Protein Data Bank (www.rcsb.org). All data reduction and refinement statistics are recorded in Table 3.

In order to improve the protein data bank statistical sliders for the HDAC6 CD1 enzyme-inhibitor complexes, the resolutions were adjusted during the final phases of refinement. The resolution of the H82F/F202Y HDAC6 CD1-TSA complex was adjusted from 1.90 Å to 2.30 Å; the resolution of the K330L HDAC6 CD1-SAHABPyne complex was adjusted from 2.15 Å to 2.40 Å; and the resolution of the K330L HDAC6 CD1-4-iodo-SAHA complex was adjusted from 1.74 Å to 1.90 Å. The electron density for each inhibitor is unambiguous.

3. Results and discussion

3.1. Crystal structure of the H82F/F202Y HDAC6 CD1–Trichostatin A complex

Active site residues in zebrafish HDAC6 CD1 and human HDAC6 CD1 are generally conserved with the exception of H82 and F202 in the zebrafish enzyme, which appear as F105 and Y225, respectively, in human HDAC6 CD1. Therefore, the double mutant H82F/F202Y was prepared to “humanize” zebrafish HDAC6 CD1 and provide a view of how these residues might influence inhibitor binding.

The 2.30 Å-resolution crystal structure of the H82F/F202Y HDAC6 CD1–Trichostatin A complex contains two monomers in the asymmetric unit. The inhibitor hydroxamate chelates the catalytic Zn^{2+} ion with bidentate coordination in each monomer (Figs. 2a,b). The Zn^{2+}-bound hydroxamate C=O group accepts a hydrogen bond from Y363, the Zn^{2+}-bound hydroxamate N-O^{-} group accepts a hydrogen bond from H192, and the hydroxamate NH group donates a hydrogen bond to H193. The linker resides in an aromatic crevice defined by Y202 and W261. The ketone carbonyl of the capping group accepts a hydrogen bonds from K330. No major conformation changes are triggered by the H82F or F202Y substitutions (Fig. 2c), and the root-mean-square (rms) deviation is 0.14 Å for 301 Cα atoms between the H82F/F202Y and wild-type HDAC6 CD1–Trichostatin A complexes.

Overall, there are no major conformation changes between monomers A and B, and the root-mean-square (r.m.s) deviation is 0.19 Å for 286 Cα atoms. However, residues 74–87 in monomer A appear predominately disordered with the exception of F82 and P83; in contrast, these residues are well-ordered in monomer B. In both monomers, 0.3–1.3 Å structural changes are observed for F82, P83, and Y202 compared to the wild-type HDAC6 CD1–Trichostatin A complex (PDB 6UO2). Remaining active site residues adopt similar conformations to those observed in the wild-type HDAC6 CD1–Trichostatin A complex.

3.2. Crystal structure of the K330L HDAC6 CD1–SAHA-BPyne complex

The pan-HDAC inhibitor SAHA-BPyne contains a SAHA scaffold derivatized with a benzophenone linker and an alkyne tag. As such, this inhibitor can be used to profile cellular HDAC through click chemistry (Salisbury and Cravatt, 2007). Until now, no crystal structure has been reported for an HDAC6 CD1 complex with SAHA or any SAHA derivative. Some HDAC6 CD1–inhibitor complexes crystallize more readily with K330L HDAC6 CD1 (Osko and Christianson, 2019), and we found this to be the case for cocrystallization trials with SAHA-BPyne.

The 2.40 Å-resolution crystal structure of the K330L HDAC6 CD1–SAHA-BPyne complex contains one monomer in the asymmetric unit. The inhibitor hydroxamate chelates the catalytic Zn^{2+} ion in bidentate fashion (Fig. 3). The SAHA amide group forms water-mediated hydrogen bonds with S150 and zinc ligand H232. Similar hydrogen bond interactions are observed with corresponding residues S531 and H614 in several HDAC6 CD2–inhibitor complexes (Osko and Christianson, 2020; Hai and Christianson, 2016; Porter et al., 2017; Bhatia et al., 2018; Mackwitz et al., 2018). The benzophenone carbonyl group forms a hydrogen bond with a water molecule that, in turn, forms hydrogen bonds with D79 and S81. The interaction with S81 has not been observed previously for inhibitor binding to

HDAC6 CD1. This residue is conserved only in human HDAC6 CD1 as S104; the corresponding residue is a histidine in human and zebrafish HDAC6 CD2. Thus, interactions with S81 can be targeted in future inhibitor designs for selective inhibition of HDAC6 CD1.

Finally, the alkyne tag of SAHA-BPyne is disordered between two conformations, and electron density is weak or absent toward the end of the tag (Fig. 3). This portion of the inhibitor makes no hydrogen bond interactions with protein residues or ordered solvent molecules.

3.3. Crystal structure of the K330L HDAC6 CD1–4-iodo-SAHA complex

The pan-HDAC inhibitor 4-iodo-SAHA is essentially isosteric with SAHA apart from the substitution of a bulky iodine atom for a hydrogen atom at the *para* position of the phenyl ring in the capping group. The 1.90 Å-resolution crystal structure of the K330L HDAC6 CD1–4-iodo-SAHA complex contains 2 monomers in the asymmetric unit. There are no major conformation changes between monomers A and B, and the rms deviation is 0.16 Å for 293 Cα atoms. The inhibitor hydroxamate chelates the catalytic Zn^{2+} ion with bidentate coordination, and the aliphatic linker resides in an aromatic crevice defined by F202 and W261 (Figs. 4a,b). As observed in the binding of SAHA-BPyne to K330L HDAC6 CD1, the amide moiety of the capping group forms water-mediated hydrogen bonds with S150 and zinc ligand H232.

Interestingly, the iodine atom of the inhibitor capping group makes a halogen bond with the carboxylate side chain of D79 in the outer active site cleft of monomer A (I---O separation = 3.1 Å). Due to conformational differences of the inhibitor capping group in monomers A and B involving a 3.3 Å shift of the iodine atom, this enzyme-inhibitor halogen bond interaction is not observed in monomer B. Electron density for the capping group is broken in monomer A and somewhat weak in monomer B, consistent with disorder. Even so, refinements were better fit with an iodo group than a hydroxyl group at the *para* position of the aromatic capping group. Residual negative density on the iodine atom in the final $|F_o| - |F_c|$ map is likely the consequence of disorder, i.e., less than full occcupancy of the electron-rich iodine atom.

Overall, there are no major conformation changes for protein atoms between the HDAC CD1 complexes with 4-iodo-SAHA and SAHA-BPyne, and the rms deviation is 0.22 Å for 329 Cα atoms between these two complexes. Superposition of these two complexes reveals that the binding of the SAHA moieties are generally similar, with slight variations in capping group conformations (Fig. 4c).

3.4. Analysis of inhibitor binding

The use of histone deacetylase inhibitors to modulate acetylation-deacetylation cycles is a validated strategy in cancer chemotherapy and is also being explored for the treatment of other diseases (Arrowsmith et al., 2012; Falkenberg and Johnstone, 2014; Dokmanovic et al., 2007; West and Johnstone, 2014). The first HDAC inhibitor to be approved for clinical use was SAHA (formulated as Vorinostat, trade name Zolinza) for the treatment of refractory cutaneous T-cell lymphoma (Richon et al., 1996; Marks, 2007; Mann et al., 2007).

However, SAHA is a pan-HDAC inhibitor, in that it inhibits most HDAC isozymes nearly equally well; thus, its use can lead to unwanted off-target effects (Duvic et al., 2007).

HDAC6 CD2 is a particularly important target for the design of selective inhibitors for treating cancer and neurodegenerative diseases owing to its biological function as a tubulin deacetylase (Hubbert et al., 2002; Zhang et al., 2003; Haggerty et al., 2003) and as a Tau deacetylase (Min et al., 2010; Cohen et al., 2011; Noack et al., 2014). The design of selective inhibitors has been guided by numerous X-ray crystallographic studies that have illuminated distinctive structural features contributing to inhibitor affinity and selectivity (recently reviewed by Osko and Christianson, 2020). However, as increasing numbers of inhibitors are being developed for inhibition of HDAC6 CD2, it is critical to understand the impact that these inhibitors may have on the catalytic domain CD1 of HDAC6.

The *in vivo* function of HDAC6 CD1 is not fully understood. Measurements made with cell extracts suggest that CD1 serves as an E3 ubiquitin ligase (Zhang et al., 2014) as well as an RNA helicase DDX3X deacetylase (Saito et al., 2019). However, the only activity that has been confirmed *in vitro* for a single-domain HDAC6 CD1 construct is as a lysine deacetylase with much narrower substrate specificity than CD2 (Hai et al., 2016; Osko et al., 2019), although CD1 substrate specificity is reported to be wider for the full-length enzyme (Kutil et al., 2019). Regardless of the elusive biological functions of HDAC6 CD1, it is important to understand how this catalytic domain accommodates bound inhibitors. The crystal structures of HDAC6 CD1 mutant complexes with pan-HDAC inhibitors reported herein represent the first step in understanding how different active site features can be taken into account to guide the design of domain-specific inhibitors.

How valid is the “humanized” zebrafish enzyme, H82F/F202Y HDAC6 CD1, as a surrogate for the actual human enzyme HDAC6 CD1? A definitive answer may be elusive due to the lack of a crystal structure of the human enzyme, but useful inferences may be drawn nonetheless from the current study. The binding conformation of the pan-HDAC inhibitor Trichostatin A in the active site of the zebrafish enzyme is unperturbed by the H82F/F202Y substitutions (Fig. 2c). In studies with another pan-HDAC inhibitor, a SAHA derivative bearing a *para*-substituted fluorescein tag designated “fl-SAHA” (Kim et al., 2015), inhibitor dissociation constants change very little from wild-type zebrafish HDAC6 CD1 (K_d = 1.6 ± 0.3 μM) to zebrafish H82F/F202Y HDAC6 CD1 (K_d = 2.9 ± 0.7 μM) (Hai and Christianson, 2016). The binding of fl-SAHA to a di-domain construct of the human enzyme in which CD2 is deactivated by mutation, H651V CD12, indicates approximately 10-fold weaker binding (K_d = 30 ± 20 μM) (Hai and Christianson, 2016). Given the general conservation of amino acids defining the active site contours of zebrafish and human HDAC6 CD1 enzymes, the similar binding conformations of Trichostatin A, and the slightly perturbed fl-SAHA binding affinities, we suggest that both wild-type and “humanized” zebrafish H82F/F202Y HDAC6 CD1 serve as valid and readily studied surrogates of human HDAC6 CD1.

We have previously observed that the K330L mutant of zebrafish HDAC6 CD1 can be more amenable to crystallization with certain inhibitors than the wild-type enzyme (Osko and Christianson, 2019). Even though this amino acid substitution makes the CD1 active site more like that of CD2, inhibitor binding is identical in the active sites of both wild-type and

mutant zebrafish CD1 enzymes. Here, the use of K330L HDAC6 CD1 enabled cocrystallization with two different SAHA derivatives, which represent the first structures of CD1 complexed with analogues of an approved drug for cancer chemotherapy. The SAHA core of each inhibitor studied binds in similar fashion (Figure 4c); intriguingly, the benzophenone proteomics tag of SAHA-BPyne maps out a region of the outer active site cleft that could be targeted in the design of a CD1-selective inhibitor, including interactions with S81 (Fig. 3b), a residue unique to CD1 in the zebrafish and human enzymes. The SAHA-BPyne inhibitor is the largest inhibitor studied to date in complex with HDAC6 CD1, so the structure of this complex reveals new information regarding the accessibility of the protein surface surrounding the active site cleft that can be targeted by a bound inhibitor.

4. Conclusions

The current work demonstrates that active site mutants of zebrafish HDAC6 CD1 enable cocrystallization with inhibitors to map out intermolecular interactions in the active site contributing to enzyme-inhibitor affinity. The active site of H82F/F202Y zebrafish HDAC6 CD1 is a more faithful mimic of the active site of human HDAC6 CD1, yet inhibitor binding conformation and affinity are quite similar between wild-type and H82F/F202Y HDAC6 enzymes. Even so, an interaction with the side chain of Y202 in human HDAC6 CD1 might confer isozyme selectivity, since this tyrosine residue is unique to human HDAC6 CD1 and the phenolic hydroxyl group protrudes into the active site.

Inhibitor binding conformations are generally identical between wild-type and K330L HDAC6 CD1, even though the K330L substitution mimics HDAC6 CD2. Interestingly, cocrystallization of wild-type zebrafish HDAC6 CD1 sometimes does not yield crystalline enzyme-inhibitor complexes, whereas cocrystallization with the active site mutants described herein yields high-quality crystals and high-resolution crystal structures. We expect that these mutants will facilitate future X-ray crystal structure determinations of HDAC6 CD1 complexes with inhibitors designed to selectively block its deacetylase function.

Acknowledgements

This work is based upon research conducted at the Northeastern Collaborative Access Team beamlines, which are funded by the National Institute of General Medical Sciences (NIGMS) from the National Institutes of Health (P30 GM124165). The Eiger 16M detector on 24-ID-E is funded by a NIH-ORIP HEI grant (S10OD021527). This research used resources of the Advanced Photon Source, a U.S. Department of Energy (DOE) Office of Science User Facility operated for the DOE Office of Science by Argonne National Laboratory under Contract No. DE-AC02-06CH11357. Additionally, this work is based on research conducted at beamline 17-ID-1 (AMX) at the National Synchrotron Light Source II, a DOE Office of Science User Facility operated for the DOE Office of Science by Brookhaven National Laboratory under Contract DE-SC0012704. The Life Science Biomedical Technology Research resource is primarily supported by the National Institutes of Health, NIGMS, through a Biomedical Technology Research Resource P41 grant (P41GM111244), and by the DOE Office of Biological and Environmental Research (KP1605010).

References

Adams PD, Afonine PV, Bunkóczi G, Chen VB, Davis IW, Echols N, Headd JJ, Hung L, Kapral GJ, Grosse-Kunstleve RW, McCoy AJ, Moriarty NW, Oeffner R, Read RJ, Richardson DC, Richardson JS, Terwilliger TC, Zwart PH, 2010 PHENIX: a comprehensive Python-based system for

macromolecular structure solution. Acta Cryst. D. Biol. Crystallogr, 66, 213–221. [PubMed: 20124702]

Allfrey VG, Faulkner R, Mirsky AE, 1964 Acetylation and methylation of histones and their possible role in the regulation of RNA synthesis. Proc. Natl. Acad. Sci. U. S. A, 51, 786–794. [PubMed: 14172992]

Arrowsmith CH, Bountra C, Fish PV, Lee K, Schapira M, 2012 Epigenetic protein families: a new frontier for drug discovery. Nat. Rev. Drug Discov, 11, 384–400. [PubMed: 22498752]

Battye TG, Kontogiannis L, Johnson O, Powell HR, Leslie AG, 2011 iMOSFLM: a new graphical interface for diffraction image processing with MOSFLM. Acta Cryst. D. Biol. Crystallogr, 67, 271–281. [PubMed: 21460445]

Bhatia S, Krieger V, Groll M, Osko JD, Reβing N, Ahlert H, Borkhardt A, Kurz T, Christianson DW, Hauer J, Hansen FK, 2018 Discovery of the first-in-class dual histone deacetylase-proteasome inhibitor. J. Med. Chem, 61, 10299–10309. [PubMed: 30365892]

Carlomagno Y, Chung DC, Yue M, Castanedes-Casey M, Madden BJ, Dunmore J, Tong J, DeTure M, Dickson DW, Petrucelli L, Cook C, 2017 An acetylation-phosphorylation switch that regulates tau aggregation propensity and function. J. Biol. Chem, 292, 15277–15286. [PubMed: 28760828]

Chen VB, Arendall WB III, Headd JJ, Keedy DA, Immormino RM, Kapral GJ, Murray LW, Richardson JS, Richardson DC, 2010 MolProbity: all-atom structure validation for macromolecular crystallography. Acta Cryst. D. Biol. Crystallogr, 66, 12–21. [PubMed: 20057044]

Choudhary C, Kumar C, Gnad F, Nielsen ML, Rehman M, Walther TC, Olsen JV, Mann M, 2009 Lysine acetylation targets protein complexes and co-regulates major cellular functions. Science, 325, 834–840. [PubMed: 19608861]

Cohen TJ, Guo JL, Hurtado DE, Kwong LK, Mills IP, Trojanowski JQ, Lee VM, 2011 The acetylation of tau inhibits its function and promotes pathological tau aggregation. Nat. Commun, 2, 252. [PubMed: 21427723]

Dokmanovic M, Clarke C, Marks PA, 2007 Histone deacetylase inhibitors: overview and perspectives. Mol. Cancer Res, 5, 981–989. [PubMed: 17951399]

Duvic M, Talpur R, Ni X, Zhang C, Hazarika P, Kelly C, Chiao JH, Reilly JF, Ricker JL, Richon VM, Frankel SR, 2007 Phase 2 trial of oral vorinostat (suberoylanilide hydroxamic acid, SAHA) for refractory cutaneous T-cell lymphoma (CTCL). Blood., 109, 31–39. [PubMed: 16960145]

Emsley P, Lohkamp B, Scott WG, Cowtan K, 2010 Features and development of Coot. Acta Cryst. D. Biol. Crystallogr, 66, 486–501. [PubMed: 20383002]

Evans PR, Murshudov GN, 2013 How good are my data and what is the resolution? Acta Cryst. D. Biol. Crystallogr, 69, 1204–1214. [PubMed: 23793146]

Falkenberg KJ, Johnstone RW, 2014 Histone deacetylases and their inhibitors in cancer, neurological diseases and immune disorders. Nat. Rev. Drug Discov, 13, 673–691. [PubMed: 25131830]

Grozinger CM, Hassig CA, Schreiber SL, 1999 Three proteins define a class of human histone deacetylases related to yeast Hda1p. Proc. Natl. Acad. Sci. U. S. A, 96, 4868–4873. [PubMed: 10220385]

Haggarty SJ, Koeller KM, Wong JC, Grozinger CM, Schreiber SL, 2003 Domain-selective small molecule inhibitor of histone deacetylase 6 (HDAC6)-mediated tubulin deacetylation. Proc. Natl. Acad. Sci. U. S. A 100, 4389–4394. [PubMed: 12677000]

Hai Y, Christianson DW, 2016 Histone deacetylase 6 structure and molecular basis of catalysis and inhibition. Nat. Chem. Biol, 12, 741–747. [PubMed: 27454933]

Hornbeck PV, Zhang B, Murray B, Kornhauser JM, Latham V, Skrzypek E, 2015 PhosphoSitePlus, 2014: mutations, PTMs and recalibrations. Nucleic Acids Res., 43, D512–D520. [PubMed: 25514926]

Hubbert C, Guardiola A, Shao R, Kawaguchi Y, Ito A, Nixon A, Yoshida M, Wang XF, Yao TP, 2002 HDAC6 is a microtubule-associated deacetylase. Nature, 417, 455–458. [PubMed: 12024216]

Kim B, Pithadia AS, Fierke CA, 2015 Kinetics and thermodynamics of metal-binding to histone deacetylase 8. Protein Sci. 24, 354–365. [PubMed: 25516458]

Kutil Z, Skultetyova L, Rauh D, Meleshin M, Snajdr I, Novakova Z, Mikesova J, Pavlicek J, Hadzima M, Baranova P, Havlinova B, Majer P, Schutkowski M, Barinka C, 2019 The unraveling of

substrate specificity of histone deacetylase 6 domains using acetylome peptide microarrays and peptide libraries. FASEB J., 33, 4035–4045. [PubMed: 30496698]

Li L, Yang XJ, 2015 Tubulin acetylation: responsible enzymes, biological functions and human diseases. Cell Mol. Life Sci, 72, 4237–4255. [PubMed: 26227334]

Lombardi PM, Cole KE, Dowling DP, Christianson DW, 2011 Structure, mechanism, and inhibition of histone deacetylases and related metalloenzymes. Curr. Opin. Struct. Biol, 21, 735–743. [PubMed: 21872466]

López JE, Sullivan ED, Fierke CA, 2016 Metal-dependent deacetylases: cancer and epigenetic regulators. ACS Chem. Biol, 11, 706–716. [PubMed: 26907466]

Mackwitz MKW, Hamacher A, Osko JD, Held J, Schöler A, Christianson DW, Kassack MU, Hansen FK, 2018 Multicomponent synthesis and binding mode of imidazo[1,2- α]pyridine-capped selective HDAC6 inhibitors. Org. Lett, 20, 3255–3258. [PubMed: 29790770]

Mann BS, Johnson JR, Cohen MH, Justice R, Pazdur R, 2007 FDA approval summary: vorinostat for treatment of advanced primary cutaneous T-cell lymphoma. Oncologist., 12, 1247–1252. [PubMed: 17962618]

Marks PA, 2007 Discovery and development of SAHA as an anticancer agent. Oncogene., 26, 1351–1356. [PubMed: 17322921]

McCoy AJ, Grosse-Kunstleve RW, Adams PD, Winn MD, Storoni LC, Read RJ, 2007 Phaser crystallographic software. J. Appl. Crystallogr, 40, 658–674. [PubMed: 19461840]

Min SW, Cho SH, Zhou Y, Schroeder S, Haroutunian V, Seeley WW, Huang EJ, Shen Y, Masliah E, Mukherjee C, Meyers D, Cole PA, Ott M, Gan L, 2010 Acetylation of tau inhibits its degradation and contributes to tauopathy. Neuron, 67, 953–966. [PubMed: 20869593]

Miyake Y, Keusch JJ, Wang L, Saito M, Hess D, Wang X, Melancon BJ, Helquist P, Gut H, Matthias P, 2016 Structural insights into HDAC6 tubulin deacetylation and its selective inhibition. Nat. Chem. Biol, 12, 748–754. [PubMed: 27454931]

Noack M, Leyk J, Richter-Landsberg C, 2014 HDAC6 inhibition results in tau acetylation and modulates tau phosphorylation and degradation in oligodendrocytes. Glia, 62, 535–547. [PubMed: 24464872]

Osko JD, Christianson DW, 2019 Structural basis of catalysis and inhibition of HDAC6 CD1, the enigmatic catalytic domain of histone deacetylase 6. Biochemistry, 58, 4912–4924. [PubMed: 31755702]

Osko JD, Christianson DW, 2020 Structural determinants of affinity and selectivity in the binding of inhibitors to histone deacetylase 6. Bioorg. Med. Chem. Lett, 30, 127023. [PubMed: 32067866]

Osko JD, Porter NJ, Narayana Reddy PA, Xiao YC, Jung M, Hooker JM, Salvino JM, Christianson DW, 2020 Exploring structural determinants of inhibitor affinity and selectivity in complexes with histone deacetylase 6. J. Med. Chem, 63, 295–308. [PubMed: 31793776]

Porter NJ, Christianson DW, 2019 Structure, mechanism, and inhibition of the zinc-dependent histone deacetylases. Curr. Opin. Struct. Biol, 59, 9–18. [PubMed: 30743180]

Porter NJ, Mahendran A, Breslow R, Christianson DW, 2017 Unusual zinc binding mode of HDAC6-selective hydroxamate inhibitors. Proc. Natl. Acad. Sci. U. S. A, 114, 13459–13464. [PubMed: 29203661]

Porter NJ, Osko JD, Diedrich D, Kurz T, Hooker JM, Hansen FK, Christianson DW, 2018 Histone deacetylase 6-selective inhibitors and the influence of capping groups on hydroxamate-zinc denticity. J. Med. Chem, 61, 8054–8060. [PubMed: 30118224]

Porter NJ, Shen S, Barinka C, Kozikowski AP, Christianson DW, 2018 Molecular basis for the selective inhibition of histone deacetylase 6 by a mercaptoacetamide inhibitor. ACS Med. Chem. Lett, 9, 1301–1305. [PubMed: 30613344]

Porter NJ, Wagner FF, Christianson DW, 2018 Entropy as a driver of selectivity for inhibitor binding to histone deacetylase 6. Biochemistry, 57, 3916–3924. [PubMed: 29775292]

Richon VM, Webb Y, Merger R, Sheppard T, Jursic B, Ngo L, Civoli F, Breslow R, Rifkind RA, Marks PA, 1996 Second generation hybrid polar compounds are potent inducers of transformed cell differentiation. Proc. Natl. Acad. Sci. U. S. A, 93, 5705–5708. [PubMed: 8650156]

Saito M, Hess D, Eglinger J, Fritsch AW, Kreysing M, Weinert BT, Choudhary C, Matthias P, 2019 Acetylation of intrinsically disordered regions regulates phase separation. Nat. Chem. Biol 15, 51–61. [PubMed: 30531905]

Salisbury CM, Cravatt BF, 2007 Activity-based probes for proteomic profiling of histone deacetylase complexes. Proc. Natl. Acad. Sci. USA, 104, 1171–1176. [PubMed: 17227860]

Shen S, Svoboda M, Zhang G, Cavasin MA, Motlova L, McKinsey TA, Eubanks JH, Bařinka C, Kozikowski AP, 2020 ACS Med. Chem. Lett, in press. 10.1021/acsmedchemlett.9b00560.

Tseng JH, Xie L, Song S, Xie Y, Allen L, Ajit D, Hong JS, Chen X, Meeker RB, Cohen TJ, 2017 The deacetylase HDAC6 mediates endogenous neuritic tau pathology. Cell Rep., 20, 2169–2183. [PubMed: 28854366]

Verdel A, Khochbin S, 1999 Identification of a new family of higher eukaryotic histone deacetylases. Coordinate expression of differentiation-dependent chromatin modifiers. J. Biol. Chem, 274, 2440–2445. [PubMed: 9891014]

Verdin E, Ott M, 2015 50 years of protein acetylation: from gene regulation to epigenetics, metabolism and beyond. Nat. Rev. Mol. Cell Biol, 16, 258–264. [PubMed: 25549891]

West AC, Johnstone RW, 2014 New and emerging HDAC inhibitors for cancer treatment. J. Clin. Invest, 124, 30–39. [PubMed: 24382387]

Winn MD, Ballard CC, Cowtan KD, Dodson EJ, Emsley P, Evans PR, Keegan RM, Krissinel EB, Leslie AGW, McCoy A, McNicholas SJ, Murshudov GN, Pannu NS, Potterton EA, Powell HR, Read RJ, Vagin A, Wilson KS, 2011 Overview of the CCP4 suite and current developments. Acta Cryst. D. Biol. Crystallogr, 67, 235–242. [PubMed: 21460441]

Zhang Y, Gilquin B, Khochbin S, Matthias P, 2006 Two catalytic domains are required for protein deacetylation. J. Biochem, 281, 2401–2404.

Zhang Y, Li N, Caron C, Matthias G, Hess D, Khochbin S, Matthias P, 2003 HDAC-6 interacts with and deacetylates tubulin and microtubules in vivo. EMBO J., 22, 1168–1179. [PubMed: 12606581]

Zhang M, Xiang S, Joo HY, Wang L, Williams KA, Liu W, Hu C, Tong D, Haakenson J, Wang C, Zhang S, Pavlovicz RE, Jones A, Schmidt K,H, Tang J, Dong H, Shan B, Fang B, Radhakrishnan R, Glazer PM, Matthias P, Koomen J, Seto E, Bepler G, Nicosia SV, Chen J, Li C, Gu L, Li GM, Bai W, Wang H, and Zhang X, 2014 HDAC6 deacetylases and ubiquitinates MSH2 to maintain proper levels of MutSα. Mol Cell 55, 31–46. [PubMed: 24882211]

Zou H, Wu Y, Navre M, Sang BC, 2006 Characterization of the two catalytic domains in histone deacetylase 6. Biochem. Biophys. Res. Commun, 341, 45–50. [PubMed: 16412385]

Synopsis Histone deacetylase 6 (HDAC6) is an emerging target for the treatment of various diseases such as cancer through selective inhibition. While the second catalytic domain has been extensively studied (HDAC6 CD2), comparatively little research has focused on the first catalytic domain (HDAC6 CD1). This work provides new structural insight regarding inhibitor binding to HDAC6 CD1 enabled by the study of active site mutants.

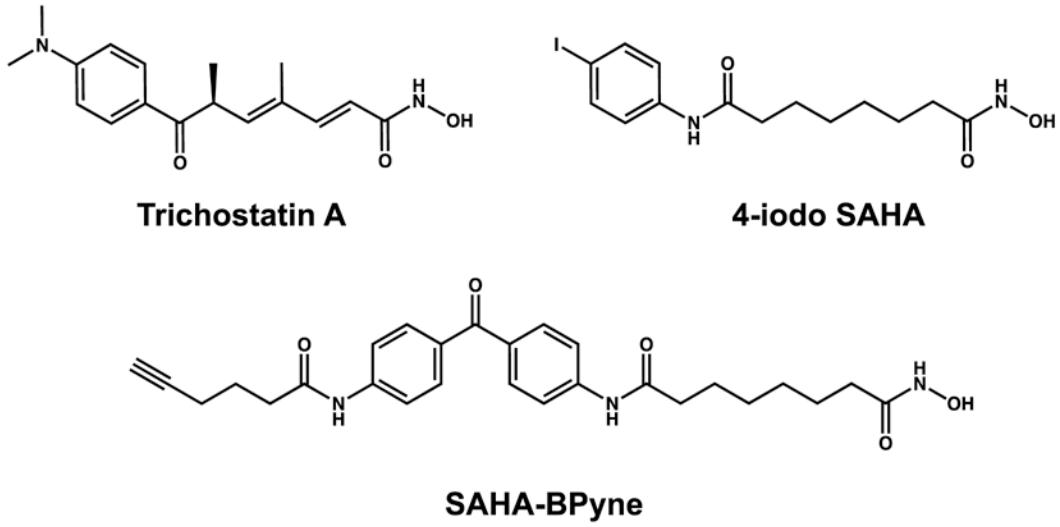

Figure 1.
Inhibitors studied in complexes with H82F/F202Y and K330L HDAC6 CD1 mutants.

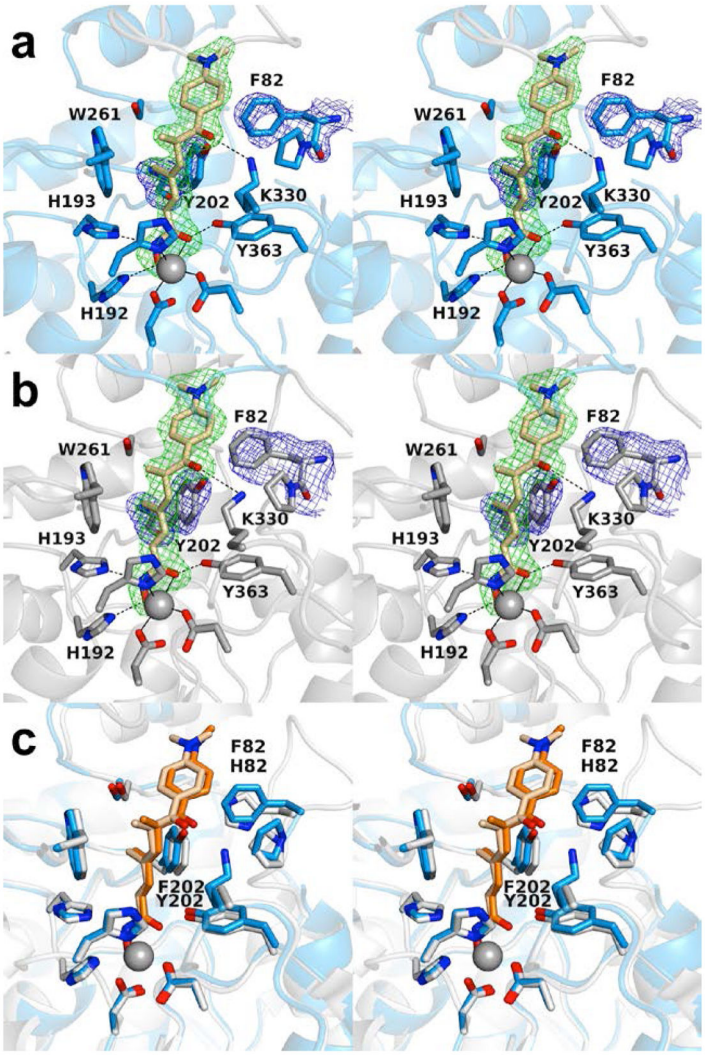

Figure 2.

Stereoviews of the H82F/F202Y HDAC6 CD1–Trichostatin A complex (PDB 6WYO). (a) Polder omit maps showing Trichostatin A bound to monomer A (contoured at 3.5 σ), F82 (contoured at 2.0 σ), and Y202 (contoured at 2.5 σ). Atoms are color-coded as follows: C = light blue (monomer A), light gray (monomer B), or wheat (inhibitor), N = blue, O = red, and Zn^{2+} = gray sphere. Metal coordination and hydrogen bond interactions are indicated by solid and dashed black lines, respectively. (b) Polder omit maps showing Trichostatin A bound to monomer B (contoured at 3.5 σ), F82 (contoured at 2.0 σ), and Y202 (contoured at 2.5 σ). Atoms are color-coded as in (a). (c) Superposition of the Trichostatin A complexes with wild-type HDAC6 CD1 (PDB 6UO2; monomer B) and H82F/F202Y HDAC6 CD1 (PDB 6WYO; monomer A). Residue 82 displays slight flexibility, consistent with the weaker electron density observed for F82 in (a) and (b). Atoms are color-coded as follows: C = light blue (H82F/F202Y HDAC6 CD1), light gray (HDAC6 CD1), wheat (Trichostatin A, bound to H82F/F202Y HDAC6 CD1) or orange (Trichostatin A, bound to wild-type HDAC6 CD1), N = blue, O = red, and Zn^{2+} = gray sphere.

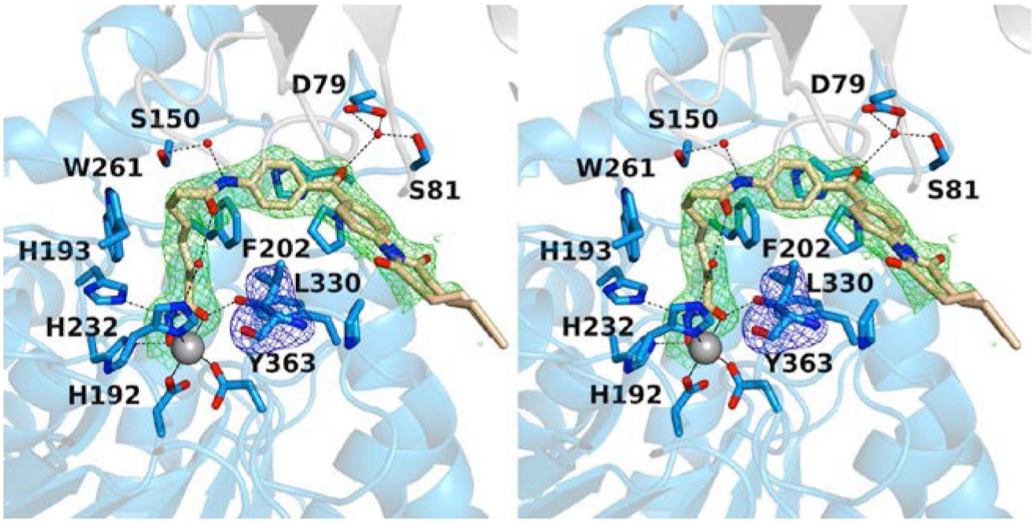

Figure 3.

Stereoview of the K330L HDAC6 CD1–SAHA-BPyne complex (PDB 6WYP). Polder omit maps showing SAHA-BPyne bound to monomer A and L330 (each contoured at 2.5 σ). Atoms are color-coded as follows: C = light blue (monomer A), light gray (symmetry mate), or wheat (inhibitor), N = blue, O = red, Zn^{2+} = gray sphere, and solvent = small red spheres. Metal coordination and hydrogen bond interactions are indicated by solid and dashed black lines, respectively.

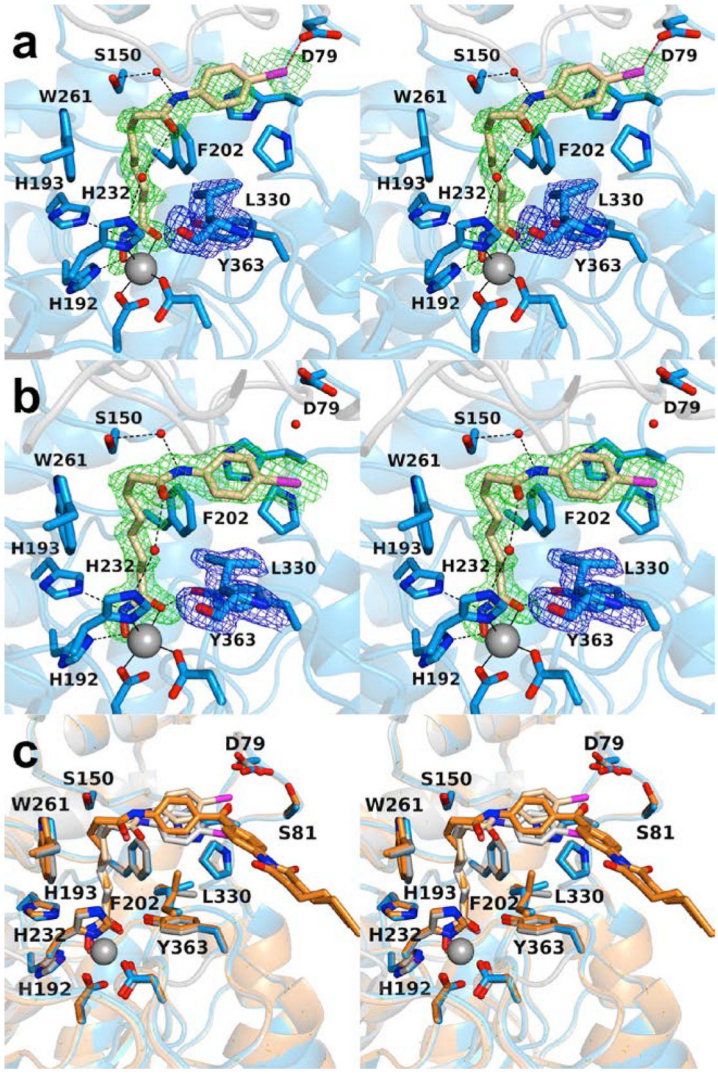

Figure 4.

Stereoviews of the K330L HDAC6 CD1–4-iodo-SAHA complex (PDB 6WYQ). (a) Polder omit maps showing 4-iodo-SAHA bound to monomer A and L330 (each contoured at 2.5 σ). Atoms are color-coded as follows: C = light blue (monomer A), light gray (monomer B), or wheat (inhibitor), N = blue, O = red, I^- = magenta, Zn^{2+} = gray sphere, and solvent = small red spheres. Metal coordination and hydrogen bond interactions are indicated by solid and dashed black lines, respectively. The halogen bond between the inhibitor iodine atom and D79 is indicated by a dashed magenta line. (b) Polder omit maps showing 4-iodo-SAHA bound to monomer B (contoured at 3.5 σ) and L330 (contoured at 3.0 σ). Atoms are color-coded as in (a), except that C = light blue for monomer B and light gray for monomer A. (c) Superposition of the K330L HDAC6 CD1 complexes with 4-iodo-SAHA (monomer A and inhibitor, blue and wheat, respectively; monomer B and inhibitor, gray and light gray, respectively) and SAHA-BPyne (protein and inhibitor, orange and dark orange, respectively) reveal that the SAHA moieties of each inhibitor bind with generally similar conformations, with slight variations in capping group conformations.

Table 1

Macromolecule production

Source organism: *Escherichia coli*.
DNA source: HDAC6 gene from *Danio rerio* (Uniprot F8W4B7; CD1 residues 61–419)
Cloning vector: pET28a
Expression vector: pET28a
Expression host: *Escherichia coli*.
Complete amino acid sequence of the construct produced (His tag sequences underlined, CD1 sequence starts with T61 (boldface); mutated amino acids are underlined in bold):
K330L HDAC6 CD1 MGSSHHHHHHSSGLVPRGSM**T**GTGLVYVDAFTRFHCLWDASHPECPARVSTVMEMLETEGLLGRCVQVEARAVTEDELLLVHTKEYVELMKSTQNMTEEELKTLAE
H82F/F202Y HDAC6 CD1 MGSSHHHHHHSSGLVPRGSM**T**GTGLVYVDAFTRFHCLWDAS**F**PECPARVSTVMEMLETEGLLGRCVQVEARAVTEDELLLVHTKEYVELMKSTQNMTEEELKTLAE

Table 2

Crystallization

Method: Sitting drop vapor diffusion
Plate type: PS MRC crystallization plate
Temperature (K): 100 K
Protein concentration: 10 mg/mL
Buffer composition of protein solution: 50 HEPES (pH 7.5), 100 mM KCl, 1 mM TCEP, 5% glycerol, and 2 mM inhibitor
Composition of reservoir solution:
TSA = 0.2 M potassium acetate and 20% PEG 3350
SAHA-BPyne = 0.2 M potassium sodium tartrate tetrahydrate and 20% PEG 3350
4-iodo-SAHA = 0.2 M magnesium chloride hexahydrate and 20% PEG 3350
Volume and ratio of drop: 1:1 ratio protein to precipitant solution
Volume of reservoir: 80 μL

Table 3

Data Collection and Refinement Statistics for HDAC6 CD1 Mutant–Inhibitor Complexes

HDAC6 CD1 Mutant **Inhibitor**	**H82F/F202Y** **Trichostatin A**	**K330L** **SAHA-BPyne**	**K330L** **4-iodo-SAHA**
Data Collection			
Beamline	APS, 24-ID-C 24-ID-C	NSLS-II, 17-ID-1 17-ID-1 (AMX)	APS, 24-ID-E 24-ID-E
Wavelength (Å)	0.98	0.92	0.98
Temperature (K)	100	100	100
Detector	PILATUS 6M-F	Dectris Eiger 9M	Dectris Eiger 16M
Wilson *B* factor (Å^2)	32	46	15
Crystal-detector distance (mm)	300	230	150
Rotation range per image (°)	0.20	0.20	0.20
Total rotation range (°)	180	180	180
Exposure time per image (s)	0.20	0.02	0.20
Space group	$P2_1$	$C22_12_1$	$P2_1$
a,b,c (Å)	53.1, 124.0, 55.0	66.0, 95.2, 119.7	53.1, 123.8, 55.1
α, β, γ (°)	90.0, 114.4, 90.0	90.0, 90.0, 90.0	90.0, 113.5, 90.0
R_{merge} [b]	0.054 (0.418)	0.190 (0.817)	0.091 (0.271)
R_{pim} [c]	0.052 (0.395)	0.119 (0.507)	0.071 (0.231)
$CC_{1/2}$ [d]	0.996 (0.792)	0.971 (0.618)	0.981 (0.829)
Redundancy	3.4 (3.2)	6.4 (6.7)	2.4 (2.3)
Completeness (%)	98.7 (98.4)	100.0 (100.0)	77.9 (80.6)
I/σ	8.9 (1.9)	4.8 (2.0)	5.2 (2.0)
Refinement			
Resolution (Å)	48.34-2.30 (2.38-2.30)	54.25-2.40 (2.49-2.40)	39.14-1.90 (1.97-1.90)
No. reflections	28350 (2842)	15104 (1483)	39267 (3884)
R_{work}/R_{free} [e]	0.170/0.232 (0.210/0.256)	0.204/0.243 (0.263/0.274)	0.177/0.223 (0.206/0.270)
No. atoms [f]			
Protein	5288	2688	5338
Ligand	50	73	46
Solvent	116	47	268
Average B factors (Å^2)			
Protein	33	47	14
Ligand	29	44	17
Solvent	31	43	18
R.m.s. deviations			
Bond lengths (Å)	0.007	0.002	0.007
Bond angles (°)	0.9	0.6	0.8
Ramachandran plot [g]			
Favored	95.53	96.63	96.30

HDAC6 CD1 Mutant **Inhibitor**	**H82F/F202Y** **Trichostatin A**	**K330L** **SAHA-BPyne**	**K330L** **4-iodo-SAHA**
Allowed	4.47	3.37	3.70
Outliers	0.00	0.00	0.00
PDB codes	6WYO	6WYP	6WYQ

[a] Values in parentheses refer to the highest-resolution shell indicated.

[b] $R_{merge} = \sum_{hkl}\sum_{i}|I_{i,hkl} - \langle I\rangle_{hkl}|/\sum_{hkl}\sum_{i}I_{i,hkl}$, where $\langle I\rangle_{hkl}$ is the average intensity calculated for reflection *hkl* from replicate measurements.

[c] $R_{p.i.m.} = (\sum_{hkl}(1/(N-1))^{1/2}\sum_{i}|I_{i,hkl} - \langle I\rangle_{hkl}|)/\sum_{hkl}\sum_{i}I_{i,hkl}$, where $\langle I\rangle_{hkl}$ is the average intensity calculated for reflection *hkl* from replicate measurements and N is the number of reflections.

[d] Pearson correlation coefficient between random half-datasets.

[e] $R_{work} = \sum||F_o| - |F_c||/\sum|F_o|$ for reflections contained in the working set. $|F_o|$ and $|F_c|$ are the observed and calculated structure factor amplitudes, respectively. R_{free} is calculated using the same expression for reflections contained in the test set held aside during refinement.

[f] Per asymmetric unit.

[g] Calculated with MolProbity.